www.sciencemag.org/content/354/6308/88/suppl/DC1

# Supplementary Materials for

## Localized seismic deformation in the upper mantle revealed by dense seismic arrays

Asaf Inbal,* Jean Paul Ampuero, Robert W. Clayton

*Corresponding author. Email: ainbal@gps.caltech.edu

Published 7 October 2016, *Science* **354**, 88 (2016)
DOI: 10.1126/science.aaf1370

**This PDF file includes:**

Materials and Methods

Location error estimation

To estimate the location uncertainty we first compute the surface seismograms due to a strike-slip point source using the frequency-wavenumber wave propagation method of *Zhu and Rivera* (2002) (49). We use a 1-D velocity model extracted from the SCEC Community Velocity Model - Harvard (45) and a local attenuation model (50) to compute the synthetic surface seismograms. Since our raw data contain only the vertical component of ground velocity, the results shown below only employ the (synthetic) vertical component of the synthetic seismograms. We visually inspected these vertical traces and found that they contain very little S-wave energy. This might be due to the fact that in our synthetic tests (as well as in the actual experiment) S-wave energy from sources of interest is predominantly up-going. This geometry as well as the relatively low S-wave velocities beneath the Long-Beach array tend to increase the P- to S-wave amplitude ratios. As in the raw data, our synthetic seismograms may contain reflections from the Moho as well as mode conversions. Our tests employ a 1-D velocity model, and thus do not reproduce the effect of Moho topography on the amplitude of reflected phases. In our simplified scenario tested here, Moho reflections due to a source located beneath the array should generally be stronger than in a more realistic case which takes into account the 3-D Moho geometry. In the back-projection procedure, strong reflections may give rise to artifacts, which may result in misidentifying strong scatterers as actual seismic sources. As is shown below, our tests demonstrate that such artifacts may defocus the back-projection images, and thus increase the location uncertainties. However, the uncertainties are within a range that exerts only minor effect on the interpretation presented in the main text.

The synthetic traces are processed in the same fashion as the real data. We spatially interpolate the seismograms, downward-continue, and back-project the migrated envelopes onto the volume beneath the array. We then add noise whose distribution is derived from the noise in back-projection images produced with the raw data, which did not contain detectable events. Our detection scheme operates on the images maximum amplitudes. Inbal et al. (2015) (9) showed that in the absence of events the amplitude of the back-projection images is log-normally distributed, and hence the logarithm of their maxima follows a Gumbel distribution.

We estimate the location uncertainty from Monte-Carlo simulations. In each simulation we perturb the amplitudes of the synthetic back-projection images with log-normally distributed, spatially uncorrelated noise, and extract the location of the node with the largest perturbed amplitude. We perform 1000 simulations and report the mean and standard deviation of the output locations. Figure S1 presents the error analysis for synthetic sources whose depth varies between 7 to 35 km. For events with $M_w > 1.5$, our procedure accurately recovers the input locations down to depth of about 27 km. The uncertainty on the location of a source located at a depth of 31 km (below the Moho in our study area) is about 3 and 1 km in vertical and horizontal directions, respectively. The location uncertainty on events with $M_w < 0.5$ at depths below 20 km is generally larger, however the majority of the smallest magnitude events in our catalog occupy shallower depths (Figure S1G). We conclude that the deepest, largest events in our catalog are in the upper mantle, that the width of the deep localized deformation zone beneath LB likely does not exceed 2 km, and that our structural inference of multiple strands beneath the Rosecrans segment is robust.

Temporal analysis

To estimate the degree of temporal clustering we divide the volume into shallow (<10 km) and deep (>25 km) depth ranges, and bin the events at 2.5x3 km, and 3x4.5 km cells, respectively. For each depth range and for each bin we compute seismicity rates by using a fixed data window according to the steps outlined in Inbal et al. (2015) (9). We resample the rate functions at 2-minute bins using linear interpolation, zero-pad the rates on both ends, compute their autocorrelation function, and stack the autocorrelations for each depth range. The autocorrelation function of a random process should appear as a zero-peaked delta function. The increase in degree of temporal clustering for shallow event clusters causes the stacked autocorrelation function to decay more gradually relative to the one computed for the deeper clusters (Figure 3C).

We use larger bins for deeper events to ensure that the number of events in these clusters is not significantly different than the size of shallow clusters. However, the total number of deep events is only about 30% of the number of shallow events, which may bias our results. In addition, some artifacts are introduced into the autocorrelation analysis due to zero-padding of short sequences. We address these issues by analyzing a synthetic catalog in which event times are drawn from a Poissonian distribution, and whose temporal distribution is similar to the distribution of the deep events clusters (i.e. about 6-7 events per cluster, with average inter-event times of about 1.5 hours). We compute the rates of each simulated sequence, and, in the same fashion as the real data, compute and stack the autocorrelation functions. The dashed black curve in Figure 3C presents the results of the analysis using 30 simulated clusters. We find that the temporal distribution of deep earthquake clusters resembles more a random, Poissonian process than the distribution of the shallow event clusters.

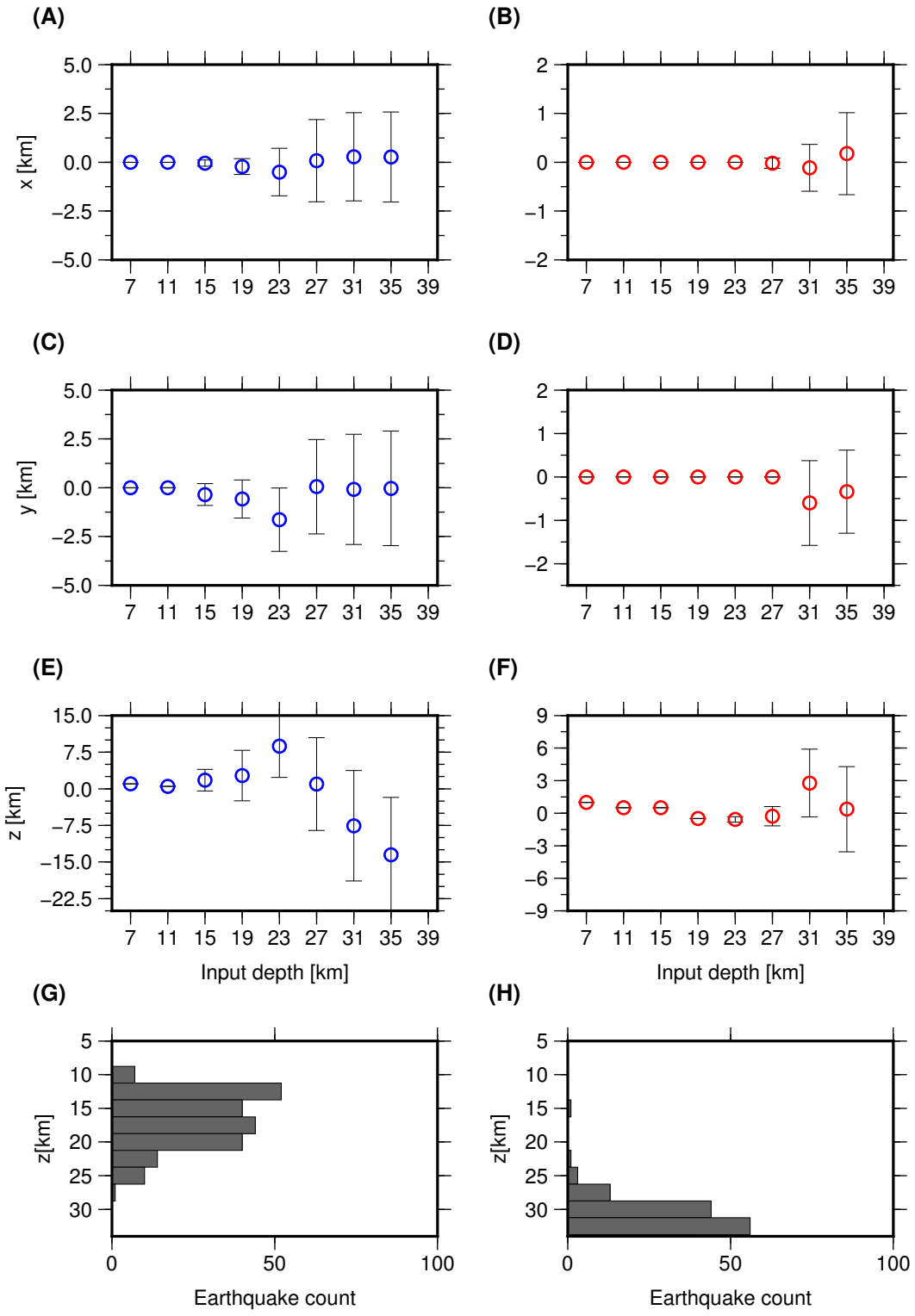


Fig. S1: The location errors derived from synthetic tests. The Left and right columns are for input sources with $M_w$=0.5 and $M_w$=1.5, respectively. For each input magnitude, we show the difference between input and output x, y, and z coordinates in panels A-B, C-D, and E-F, respectively. The error bars indicate 1-sigma uncertainties. Focal depth distributions in LB for events with $0.4 < M_w < 0.5$, and $M_w > 1.5$ are shown in panels G and H, respectively.

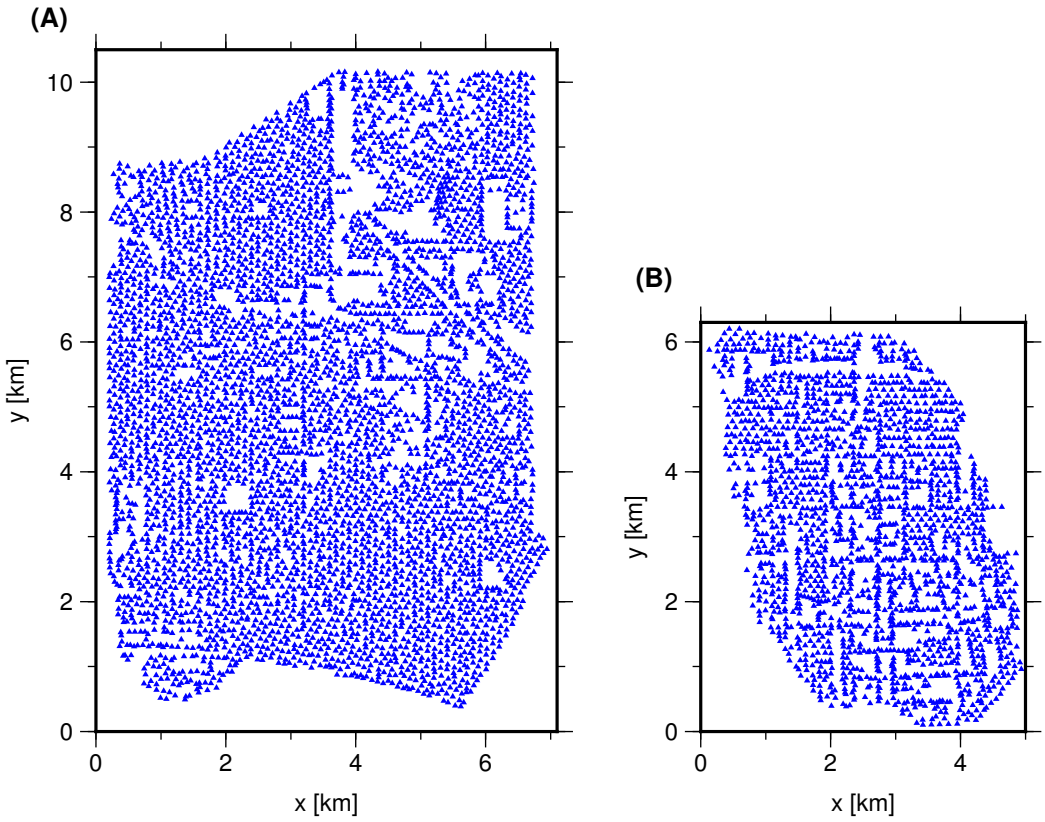


Fig. S2: The arrays layout. (A) The Long-Beach array. (B) The Rosecrans array. The blue triangles indicate locations of sensors.

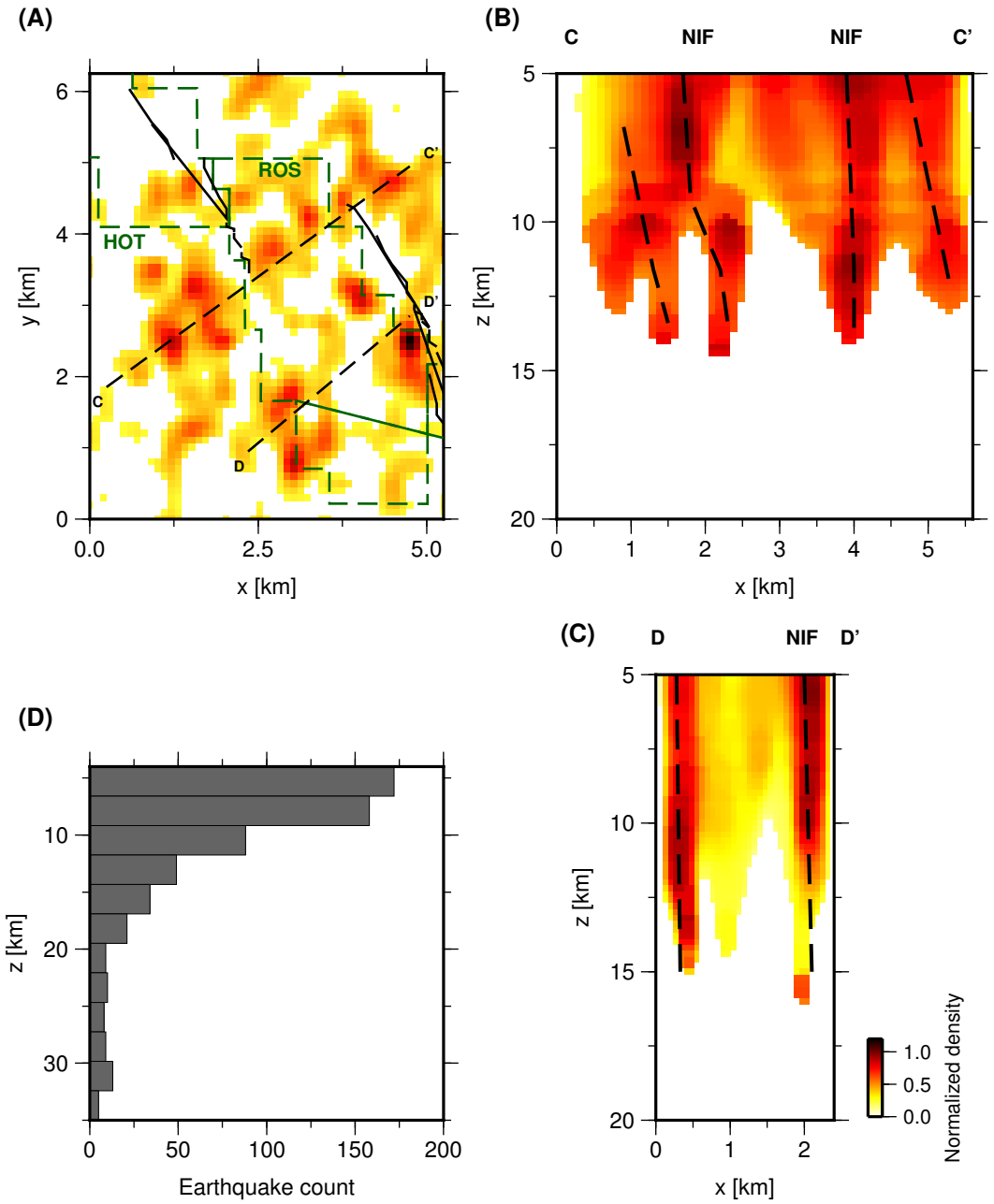


Fig. S3: The spatial distribution of earthquake density from a catalog spanning 25 nights of the Rosecrans dataset. (A) Rosecrans catalog event density for the depth range 5-35 km. (B)-(C) A vertical cross-section along lines C-C' and D-D' in panel E. We normalized the densities in panel A by the maximum value, and the density in the cross-sections by the maximum in 2 km depth bins. (D) The event depth distribution. The location of the NIF surface trace, and inferred faults are indicated by solid and dashed black lines, respectively. The local oilfields are indicated by green dashed lines. ROS: Rosecrans, HOT: Howard Townsite.

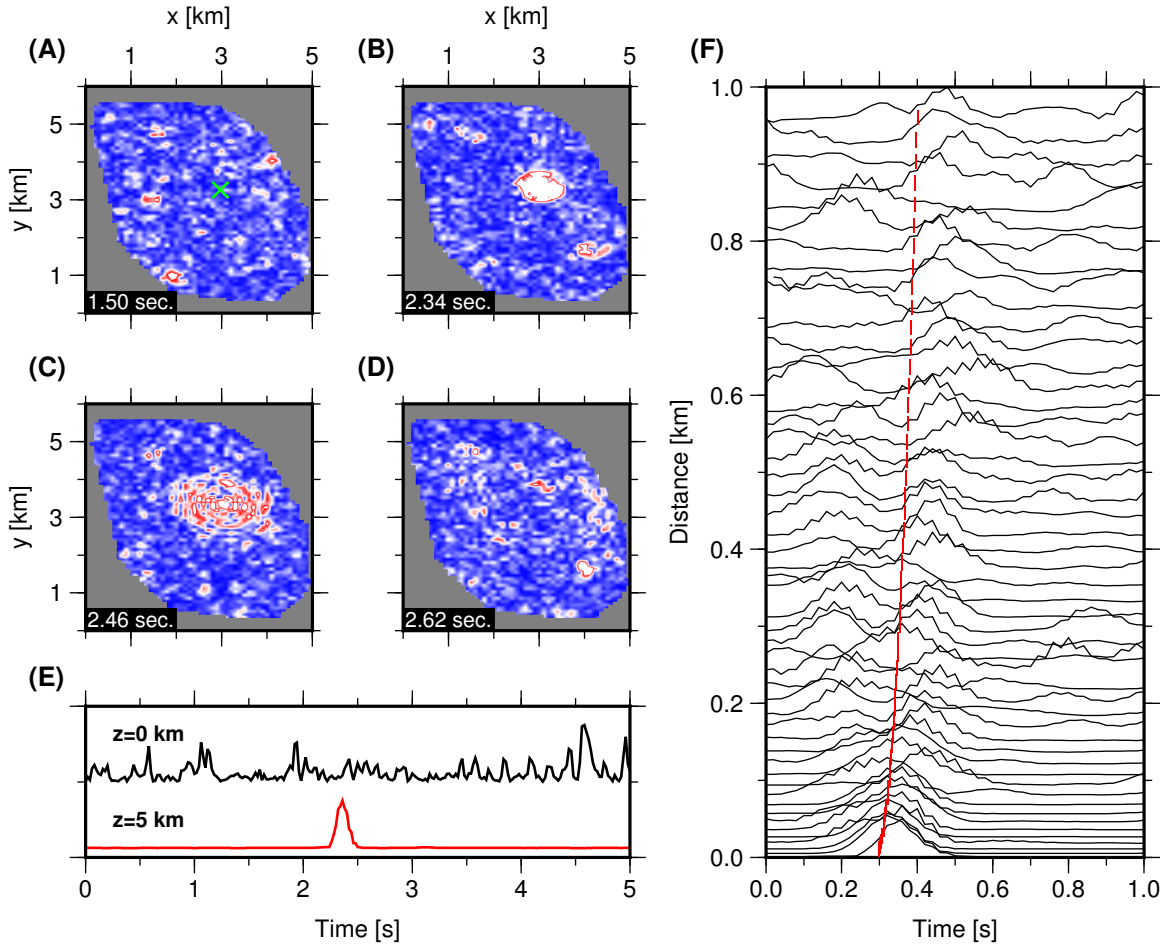


Fig. S4: The ground velocity amplitudes in Rosecrans due to a $M_w$=0.4. (A)-(D) Velocity envelopes of downward-continued (5 km) waveforms as a function of position. (E) Velocity envelopes at the surface (black) and at 5 km depth (red) for 2 collocated points within the array that are indicated by the green cross in panel A. (F) Downward-continued envelopes. Vertical axis indicates epicentral distance. Traces are normalized by their maximum. Red bars indicate expected P-wave arrival times.

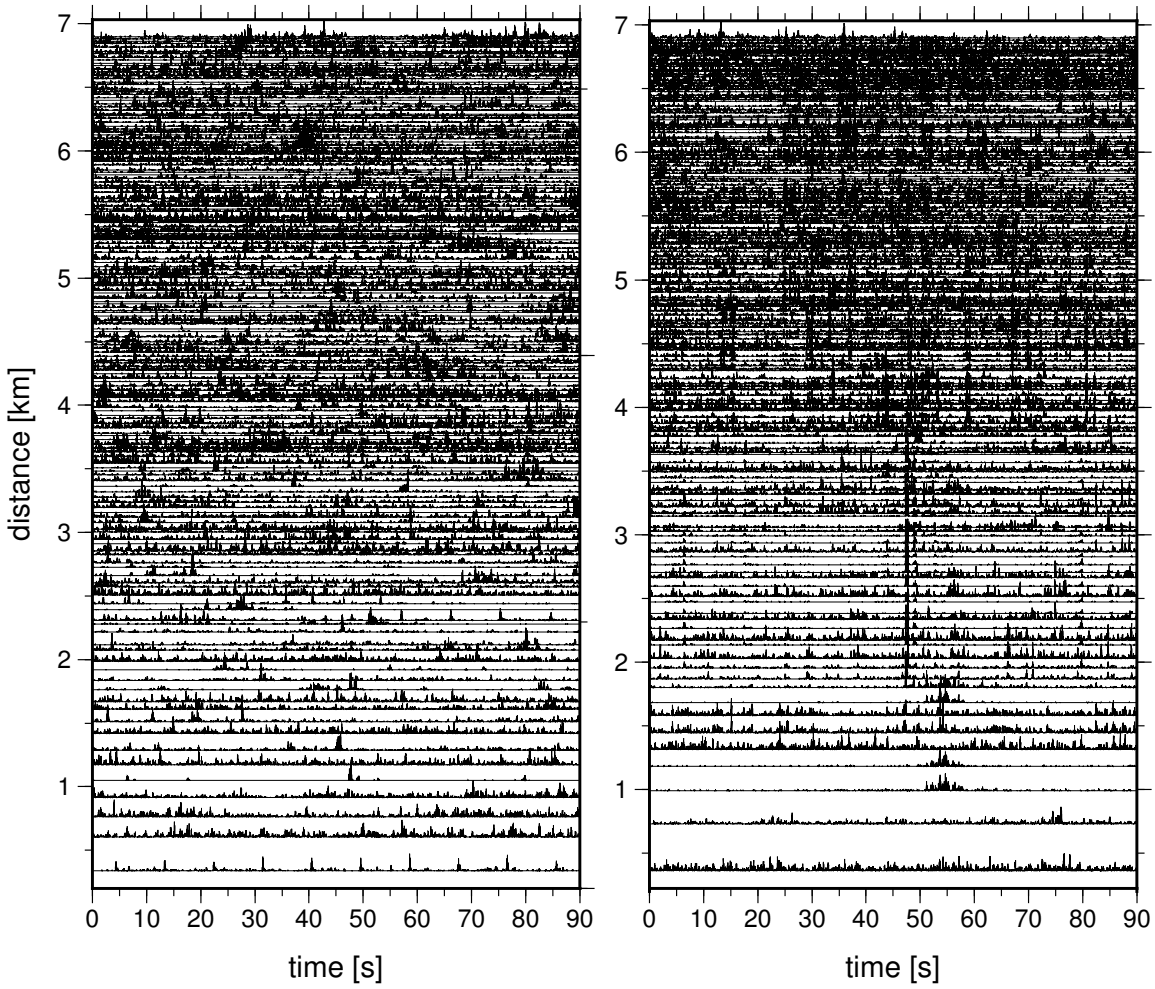


Fig. S5: Amplitude as a function of time for traces containing a local swarm in which the largest event is a $M_w$ = 1.0 whose P-waves arrive between 45-55 seconds. Left: Waveform envelopes before downward-continuation. Right: After downward continuation to a depth of 5 km. Vertical axis indicates epicentral distance. Traces are normalized by their maximum.

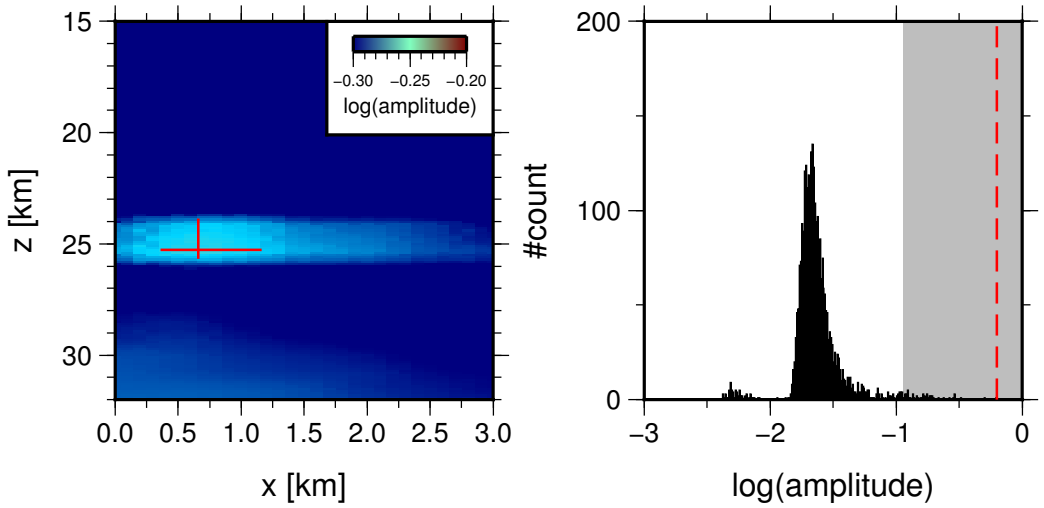


Fig. S6: Back-projected stack amplitudes for the $M_w$=1.0 event shown in Figure S5. Left: Log of maximum stack power for a 5-second window projected onto a vertical cross-section oriented EW. Right: Histogram of log of stack maxima in a 4-hour window around the detected event. Grey rectangle indicates region of acceptance, and red dashed curve indicates amplitude of log of the stack maxima for the detection window in the left panel.

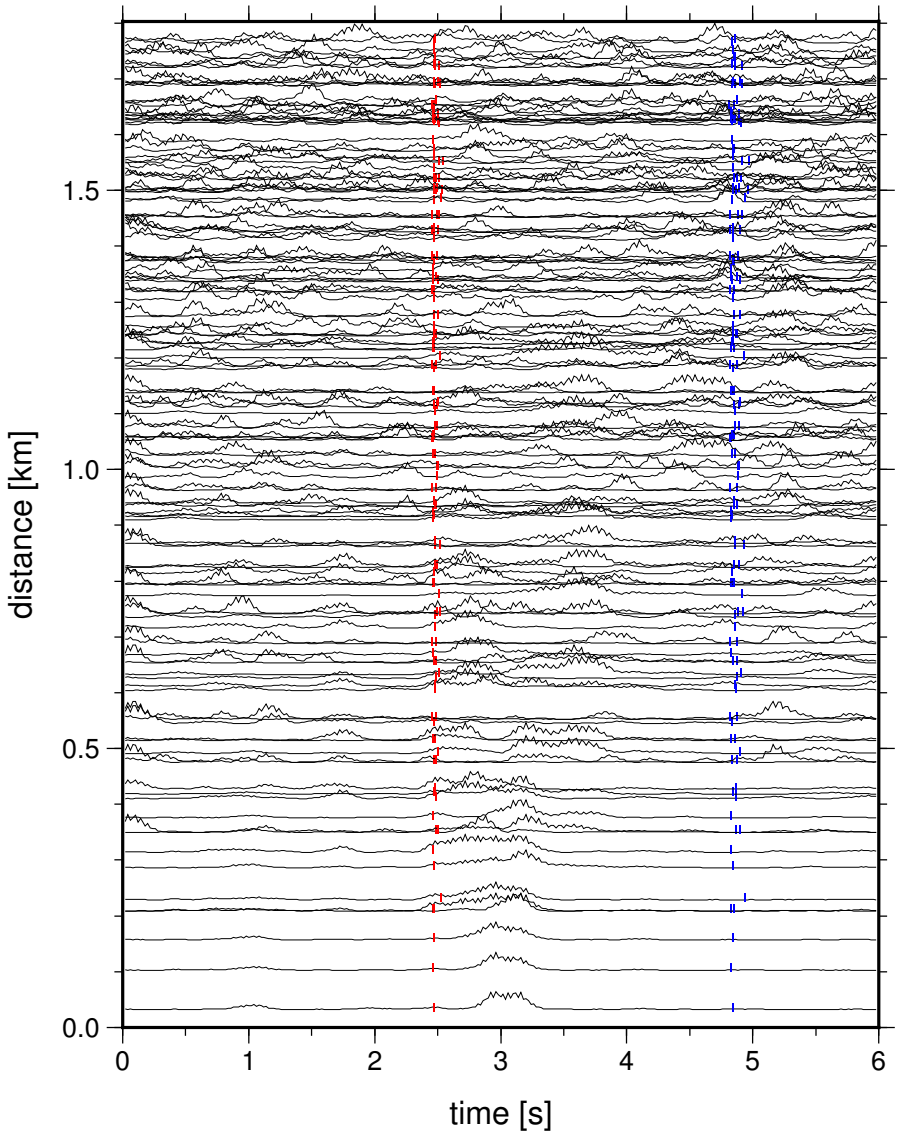


Fig. S7: The amplitude as a function of time for downward-continued traces containing a $M_w = 1.5$ event located at depth of 27 km beneath the LB array. Vertical axis indicates epicentral distance. Traces are normalized by their maximum. Red and blue bars indicate expected P- and S-wave arrival times.

**References and Notes**


1. A. Maggi, J. Jackson, D. McKenzie, K. Priestley, Earthquake focal depths, effective elastic thickness, and the strength of the continental lithosphere. *Geology* **28**, 495–498 (2000). doi:10.1130/0091-7613(2000)28<495:EFDEET>2.0.CO;2

2. R. Bürgmann, G. Dresen, Rheology of the Lower crust and upper mantle: Evidence from rock mechanics, geodesy, and field observations. *Annu. Rev. Earth Planet. Sci.* **36**, 531–567 (2008). doi:10.1146/annurev.earth.36.031207.124326

3. C. Thurber *et al*., Three-dimensional compressional wavespeed model, earthquake relocations, and focal mechanisms for the Parkfield, California, region. *Bull. Seismol. Soc. Am.* **96**, S38–S49 (2006). doi:10.1785/0120050825

4. M. Kahraman, D. G. Cornwell, D. A. Thompson, S. Rost, G. A. Houseman, N. Türkelli, U. Teoman, S. Altuncu Poyraz, M. Utkucu, L. Gülen, Crustal-scale shear zones and heterogeneous structure beneath the North Anatolian Fault Zone, Turkey, revealed by a high-density seismometer array. *Earth Planet. Sci. Lett.* **430**, 129–139 (2015). doi:10.1016/j.epsl.2015.08.014

5. J. H. Shaw, A. Plesch, C. Tape, M. P. Suess, T. H. Jordan, G. Ely, E. Hauksson, J. Tromp, T. Tanimoto, R. Graves, K. Olsen, C. Nicholson, P. J. Maechling, C. Rivero, P. Lovely, C. M. Brankman, J. Munster, Unified structural representation of the southern California crust and upper mantle. *Earth Planet. Sci. Lett.* **415**, 1–15 (2015). doi:10.1016/j.epsl.2015.01.016

6. R. J. Norris, A. F. Cooper, Very high strains recorded in mylonites along the Alpine Fault, New Zealand: Implications for the deep structure of plate boundary faults. *J. Struct. Geol.* **25**, 2141–2157 (2003). doi:10.1016/S0191-8141(03)00045-2

7. J. C. White, Paradoxical pseudotachylyte – Fault melt outside the seismogenic zone. *J. Struct. Geol.* **38**, 11–20 (2012). doi:10.1016/j.jsg.2011.11.016

8. J. R. Rice, Heating and weakening of faults during earthquake slip. *J. Geophys. Res.* **111**, B05311 (2006). doi:10.1029/2005JB004006

9. A. Inbal, R. Clayton, J.-P. Ampuero, Imaging widespread seismicity at midlower crustal depths beneath Long Beach, CA, with a dense seismic array: Evidence for a depth-dependent earthquake size distribution. *Geophys. Res. Lett.* **42**, 6314–6323 (2015). doi:10.1002/2015GL064942

10. A. S. Bryant, L. M. Jones, Anomalously deep crustal earthquakes in the Ventura Basin, southern California. *J. Geophys. Res.* **97**, 437–447 (1992). doi:10.1029/91JB02286

11. H. Magistrale, Relative contributions of crustal temperature and composition to controlling the depth of earthquakes in southern California. *Geophys. Res. Lett.* **29**, 87-1–87-4 (2002). doi:10.1029/2001GL014375

12. E. Hauksson, Crustal geophysics and seismicity in southern California. *Geophys. J. Int.* **186**, 82–98 (2011). doi:10.1111/j.1365-246X.2011.05042.x

13. L. C. Price, M. J. Pawlewicz, T. A. Daws, Organic metamorphism in the California petroleum basins; Chapter A, Rock-Eval and vitrinite reflectance. (U.S. Geological Survey Bulletin 2174-A, 1999).

14. E. Hauksson, W. Yang, P. M. Shearer, Waveform relocated earthquake catalog for southern California (1981 to June 2011). *Bull. Seismol. Soc. Am.* **102**, 2239–2244 (2012). doi:10.1785/0120120010

15. L. B. Grant, J. T. Waggoner, T. K. Rockwell, C. vonStein, Paleoseismicity of the north branch of the Newport-Inglewood fault zone in Huntington Beach, California, from cone penetrometer test data. *Bull. Seismol. Soc. Am.* **87**, 277–293 (1997).

16. D. L. Kohlstedt, B. Evans, S. J. Mackwell, Strength of the lithosphere: Constraints imposed by laboratory experiments. *J. Geophys. Res.* **100**, 17587–17602 (1995). doi:10.1029/95JB01460

17. G. Hirth, N. M. Beeler, The role of fluid pressure on frictional behavior at the base of the seismogenic zone. *Geology* **43**, 223–226 (2015). doi:10.1130/G36361.1

18. E. O. Lindsey, Y. Fialko, Geodetic slip rates in the southern San Andreas Fault system: Effects of elastic heterogeneity and fault geometry. *J. Geophys. Res.* **118**, 689–697 (2013). doi:10.1029/2012JB009358

19. J. Gazdag, Wave equation migration with the phase-shift method. *Geophys.* **43**, 1342–1351 (1978). doi:10.1190/1.1440899

20. IRIS, Incorporated Research Institutions for Seismology; www.iris.edu/hq.

21. Materials and methods are available as supplementary materials on *Science* Online.

22. J. Crouch, J. Suppe, Late Cenozoic tectonic evolution of the Los Angeles basin and inner California borderland: A model for core complex-like crustal extension. *Geol. Soc. Am. Bull.* **105**, 1415–1434 (1993). doi:10.1130/0016-7606(1993)105<1415:LCTEOT>2.3.CO;2

23. T. L. Wright, "Structural geology and tectonic evolution of the Los Angeles Basin, California," in American Association of Petroleum Geologists Memoir 52, K. T. Biddle, Ed. (1991), pp. 35–134.

24. B. M. Kennedy *et al.*, Mantle fluids in the San Andreas Fault system, California. *Science* **278**, 1278–1281 (1997). doi:10.1126/science.278.5341.1278

25. J. R. Boles, G. Garven, H. Camacho, J. E. Lupton, Mantle helium along the Newport-Inglewood fault zone, Los Angeles basin, California: A leaking paleo-subduction zone. *Geochem. Geophys. Geosyst.* **16**, 2364–2381 (2015). doi:10.1002/2015GC005951

26. V. Lekic, S. W. French, K. M. Fischer, Lithospheric thinning beneath rifted regions of Southern California. *Science* **334**, 783–787 (2011).doi:10.1126/science.1208898 Medline

27. C. H. Scholz, On the stress dependence of the earthquake *b* value. *Geophys. Res. Lett.* **42**, 1399–1402 (2015). doi:10.1002/2014GL062863

28. C. H. Scholz, The frequency-magnitude relation of microfracturing in rock and its relation to earthquakes. *Bull. Seismol. Soc. Am.* **58**, 399–415 (1968).

29. M. Spada, T. Tormann, S. Wiemer, B. Enescu, Generic dependence of the frequency-size distribution of earthquakes on depth and its relation to the strength profile of the crust. *Geophys. Res. Lett.* **40**, 709–714 (2013). doi:10.1029/2012GL054198

30. T. Watanabe, Y. Hiramatsu, K. Obara, Scaling relationship between the duration and the amplitude of non-volcanic deep low-frequency tremors. *Geophys. Res. Lett.* **34**, L07305 (2007). doi:10.1029/2007GL029391

31. D. R. Shelly, J. L. Hardebeck, Precise tremor source locations and amplitude variations along the lower-crustal central San Andreas Fault. *Geophys. Res. Lett.* **37**, L14301 (2010). doi:10.1029/2010GL043672

32. J. R. Sweet, K. C. Creager, H. Houston, A family of repeating low-frequency earthquakes at the downdip edge of tremor and slip. *Geochem. Geophys. Geosyst.* **15**, 3713–3721 (2014). doi:10.1002/2014GC005449

33. M. G. Bostock, A. M. Thomas, G. Savard, L. Chuang, A. M. Rubin, Magnitudes and moment-duration scaling of low-frequency earthquakes beneath southern Vancouver Island. *J. Geophys. Res.* **120**, 6329–6350 (2015)..

34. B. Schmandt, R. W. Clayton, Analysis of teleseismic *P* waves with a 5200-station array in Long Beach, California: Evidence for an abrupt boundary to Inner Borderland rifting. *J. Geophys. Res.* **118**, 5320–5338 (2013). doi:10.1002/jgrb.50370

35. E. Hauksson, Crustal structure and seismicity distribution adjacent to the Pacific and North America plate boundary in southern California. *J. Geophys. Res.* **105**, 13875–13903 (2000). doi:10.1029/2000JB900016

36. T. Romanyuk, W. D. Mooney, S. Detweiler, Two lithospheric profiles across southern California derived from gravity and seismic data. *J. Geodyn.* **43**, 274–307 (2007). doi:10.1016/j.jog.2006.09.011

37. E. Hauksson, Seismotectonics of the Newport-Inglewood fault zone in the Los Angeles basin, southern California. *Bull. Seismol. Soc. Am.* **77**, 539–561 (1987).

38. R. Porter, G. Zandt, N. McQuarrie, Pervasive lower-crustal seismic anisotropy in Southern California: Evidence for underplated schists and active tectonics. *Lithosphere* **3**, 201–220 (2011). doi:10.1130/L126.1

39. P. Audet, Layered crustal anisotropy around the San Andreas Fault near Parkfield, California. *J. Geophys. Res.* **120**, 3527–3543 (2015). doi:10.1002/2014JB011821

40. D. S. H. King, C. Marone, Frictional properties of olivine at high temperature with applications to the strength and dynamics of the oceanic lithosphere. *J. Geophys. Res.* **117**, B12203 (2012).

41. E. K. Mitchell, Y. Fialko, K. M. Brown, Frictional properties of gabbro at conditions corresponding to slow slip events in subduction zones. *Geochem. Geophys. Geosyst.* **16**, 4006–4020 (2015). doi:10.1002/2015GC006093

42. T. Ueda, M. Obata, G. Di Toro, K. Kanagawa, K. Ozawa, Mantle earthquakes frozen in mylonitized ultramafic pseudotachylytes of spinel-lherzolite facies. *Geology* **36**, 607–610 (2008). doi:10.1130/G24739A.1

43. A. K. Matysiak, C. A. Trepmann, Crystal–plastic deformation and recrystallization of peridotite controlled by the seismic cycle. *Tectonophys.* **530–531**, 111–127 (2012). doi:10.1016/j.tecto.2011.11.029

44. A. J. Getsinger, G. Hirth, H. Stunitz, E. T. Goergen, Influence of water on rheology and strain localization in the lower continental crust. *Geochem. Geophys. Geosyst.* **14**, 2247–2264 (2013). doi:10.1002/ggge.20148

45. J. H. Shaw *et al*., Unified Structural Representation of the southern California crust and upper mantle. *Earth Planet. Sci. Lett.* **415**, 1–15 (2015). doi:10.1016/j.epsl.2015.01.016

46. C. Tape, A. Plesch, J. H. Shaw, H. Gilbert, Estimating a continuous Moho surface for the California Unified Velocity Model. *Seismol. Res. Lett.* **83**, 728–735 (2012). doi:10.1785/0220110118

47. Y. Ma, R. Clayton, Structure of the Los Angeles Basin from ambient noise and receiver functions. *Geophys. J. Int.* **206**, 1645–1651 (2016). doi:10.1093/gji/ggw236

48. Z. Yan, R. W. Clayton, Regional mapping of the crustal structure in southern California from receiver functions. *J. Geophys. Res.* **112**, B05311 (2007). doi:10.1029/2006JB004622

49. L. P. Zhu, L. A. Rivera, A note on the dynamic and static displacements from a point source in multilayered media. *Geophys. J. Int.* **148**, 619–627 (2002). doi:10.1046/j.1365-246X.2002.01610.x

50. E. Hauksson, P. M. Shearer, Attenuation models ($Q_P$ and $Q_S$) in three dimensions of the southern California crust: Inferred fluid saturation at seismogenic depths. *J. Geophys. Res.* **111**, B05302 (2006). doi:10.1029/2005JB003947